The Astrophysical Journal, 832:139 (16pp), 2016 December 1 doi:10.3847/0004-637X/832/2/139

OPTICAL AND ULTRAVIOLET OBSERVATIONS OF THE VERY YOUNG TYPE IIP SN 2014cx IN NGC 337

Fang Huang[1], Xiaofeng Wang[1], Luca Zampieri[2], Maria Letizia Pumo[3], Iair Arcavi[4,5], Peter J. Brown[6], Melissa L. Graham[7], Alexei V. Filippenko[7], WeiKang Zheng[7], Griffin Hosseinzadeh[4], D. Andrew Howell[4,8], Curtis McCully[4], Liming Rui[1], Stefano Valenti[9], Tianmeng Zhang[10], Jujia Zhang[11,12], Kaicheng Zhang[1], and Lifan Wang[6]

[1] Physics Department and Tsinghua Center for Astrophysics, Tsinghua University, Beijing, 100084, China; huangfang@mail.tsinghua.edu.cn, wang_xf@mail.tsinghua.edu.cn
[2] INAF-Osservatorio Astronomico di Padova, Vicolo dell'Osservatorio 5, I-35122 Padova, Italy
[3] INAF-Osservatorio Astronomico di Palermo "Giuseppe S. Vaiana," Piazza del Parlamento 1, I-90134 Palermo, Italy
[4] Las Cumbres Observatory Global Telescope Network, 6740 Cortona Drive, Suite 102, Goleta, CA 93117, USA
[5] Kavli Institute for Theoretical Physics, Kohn Hall, University of California, Santa Barbara, CA 93106-4030, USA
[6] George P. and Cynthia Woods Mitchell Institute for Fundamental Physics & Astronomy, Texas A&M University, Department of Physics and Astronomy, 4242 TAMU, College Station, TX 77843, USA
[7] Department of Astronomy, University of California, Berkeley, CA 94720-3411, USA
[8] Department of Physics, University of California, Santa Barbara, Broida Hall, Mail Code 9530, Santa Barbara, CA 93106-9530, USA
[9] Department of Physics, University of California, Davis, CA 95616, USA
[10] Key Laboratory of Optical Astronomy, National Astronomical Observatories, Chinese Academy of Sciences, Beijing 100012, China
[11] Yunnan Observatories, Chinese Academy of Sciences, Kunming 650011, China
[12] Key Laboratory for the Structure and Evolution of Celestial Objects, Chinese Academy of Sciences, Kunming 650216, China

Received 2016 July 7; revised 2016 September 1; accepted 2016 September 3; published 2016 November 23

ABSTRACT

Extensive photometric and spectroscopic observations are presented for SN 2014cx, a Type IIP supernova (SN) exploding in the nearby galaxy NGC 337. The observations are performed in optical and ultraviolet bands, covering from −20 to +400 days from the peak light. The stringent detection limit from prediscovery images suggests that this supernova was actually detected within about one day after explosion. Evolution of the very early time light curve of SN 2014cx is similar to that predicted from a shock breakout and post-shock cooling decline before reaching the optical peak. Our photometric observations show that SN 2014cx has a plateau duration of ~100 days, an absolute V-band magnitude of ~ -16.5 mag at $t \approx 50$ days, and a nickel mass of 0.056 ± 0.008 $M_{\odot}$. The spectral evolution of SN 2014cx resembles that of normal SNe IIP like SN 1999em and SN 2004et, except that it has a slightly higher expansion velocity (~4200 km s^{-1} at 50 days). From the cooling curve of photospheric temperature, we derive that the progenitor has a pre-explosion radius of ~640 $R_{\odot}$, consistent with those obtained from SuperNova Explosion Code modeling (~620 $R_{\odot}$) and hydrodynamical modeling of the observables (~570 $R_{\odot}$). Moreover, the hydrodynamical simulations yield a total explosion energy of $\sim 0.4 \times 10^{51}$ erg, and an ejected mass of ~8 $M_{\odot}$. These results indicate that the immediate progenitor of SN 2014cx is likely a red supergiant star with a mass of ~10 $M_{\odot}$.

Key words: galaxies: individual (NGC 337) – supernovae: general – supernovae: individual (SN 2014cx)

1. INTRODUCTION

Type IIP supernovae (SNe IIP) represent the most common subtype of stellar explosions, constituting about one-third of all SNe (Li et al. 2011). This subtype of SNe is thought to arise from core-collapse (CC) explosions of massive red supergiants (RSGs) with an initial mass of 8–25 $M_{\odot}$ according to theoretical models of stellar evolution (Heger et al. 2003). On the other hand, direct analyses of supernova position on pre-explosion images give a much narrower range for the progenitor mass, e.g., 8.5–16.5 $M_{\odot}$ (Li et al. 2007; Smartt 2009). Compared to other CC SNe, SNe IIP are characterized by prominent hydrogen features in their optical spectra (e.g., Filippenko 1997) and an extended plateau phase in their light curves. During the plateau phase, their luminosity remains almost constant as a result of the energy balance between the hydrogen recombination and expansion cooling. The plateau feature distinguishes SNe IIP from the Type IIL subclass, for which the light curve exhibits a linear decline (in mag day^{-1}) after the peak (Barbon et al. 1979). Recent statistical analyses show that the light-curve properties of SNe II may have a continuous distribution (e.g., Anderson et al. 2014; Sanders et al. 2015; Valenti et al. 2016), although there are also studies suggesting a distinct division between Type IIP and IIL SNe (Arcavi et al. 2012; Faran et al. 2014a, 2014b).

Over the years, numerous SNe IIP have been well studied, such as SN 1999em (Leonard et al. 2002), SN 2004et (Sahu et al. 2006), SN 2005cs (Pastorello et al. 2009), and SN 2013ej (Huang et al. 2015). These studies reveal a large spread in luminosities, plateau durations, expansion velocities, and nickel masses for SNe IIP (e.g., Hamuy 2003), which can be well understood with current explosion models (e.g., Kasen & Woosley 2009; Dessart et al. 2010; Pumo & Zampieri 2011, 2013). Nevertheless, early time observations are still sparse for SNe IIP, which are vital to constrain the explosion time and hence determine the properties of their progenitor stars (Nadyozhin 2003; Smartt et al. 2009). In particular, very early light curves of SNe IIP may be affected by a short, sharp blast of light as a result of shock breakout of the stellar surface, as predicted in massive-star core-collapse explosions (Falk & Arnett 1977; Klein & Chevalier 1978). SN 2014cx represents such a CC SN that is captured within about one day after the explosion.

SN 2014cx was independently discovered on UT 2014 September 2 by Nakano et al. (2014) and Holoien et al. (2014) in the nearby SBd galaxy NGC 337. Based on the astrometry

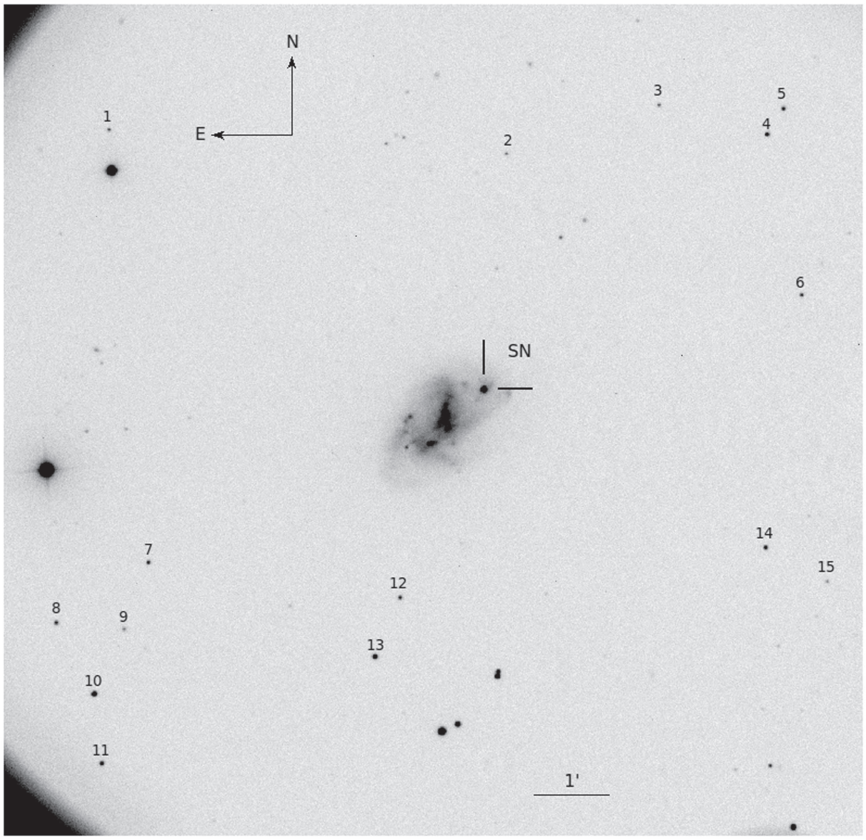

Figure 1. SN 2014cx in NGC 337. This *R*-band image was taken on 2014 October 25 with the 80 cm Tsinghua-NAOC Telescope. SN 2014cx and the 15 local sequence stars are marked.

from the USNO-A2.0 Catalog (Monet 1998), the J2000 coordinates of the SN are derived as $\alpha = 00^{\mathrm{h}}59^{\mathrm{m}}47^{\mathrm{s}}.83$ and $\delta = -07^{\circ}34'19''.3$, approximately $21''.7$ N and $33''.7$ W from the center of NGC 337 (Holoien et al. 2014). SN 2014cx was reported as a young SN II based on both optical (Elias-Rosa et al. 2014) and near-infrared (NIR; Morrell et al. 2014) spectra taken at about one day after the discovery. It was further classified as a Type IIP event according to the photometric observations by Andrews et al. (2015). We note that another SN IIP, SN 2011dq, also exploded in NGC 337. The distance to NGC 337 is estimated to be 18.0 ± 3.6 Mpc (distance modulus $\mu = 31.27 \pm 0.43$ mag) by the Tully–Fisher method (Sorce et al. 2014); here we adopt this value for SN 2014cx.

In this work, we present the results of our optical and UV observations of the Type IIP supernova SN 2014cx that was discovered at a very young age. The observations and data reduction are addressed in Section 2, the photometric evolution and spectroscopic evolution are described in Sections 3 and 4, respectively, and analysis of the progenitor properties of SN 2014cx via the photospheric temperature cooling curve and hydrodynamical modeling is given in Section 5. The main results are summarized in Section 6.

2. OBSERVATIONS AND DATA REDUCTION

2.1. *Photometry*

2.1.1. *Optical Observations*

We started the *UBVRI* follow-up campaign with the 0.8 m Tsinghua University-NAOC Telescope (hereafter TNT) at Xinglong Observatory in China (Wang et al. 2008; Huang et al. 2012). The TNT monitoring of SN 2014cx started on 2014 September 15 and continued until 2015 January 31. High-cadence Johnson *BV* and Sloan *gri* monitoring was conducted using the 1.0 m telescopes in the Las Cumbres Observatory Global Telescope network (hereafter LCOGT; Brown et al. 2013). The LCOGT data cover 2014 September 3 through 2015 September 17. In addition, 55 epochs of unfiltered data were collected with the 0.76 m Katzman Automatic Imaging Telescope (KAIT; Filippenko et al. 2001), extending to 2015 January 5.

All of the images were reduced with standard IRAF[13] routines. Point-spread-function (PSF) photometry was performed on TNT and LCOGT data using the SNOoPy package.[14] KAIT data were reduced using a PSF-based image-reduction pipeline (Ganeshalingam et al. 2010). The SN instrumental magnitudes were calibrated using 15 field stars (marked in Figure 1) from the Sloan Digital Sky Survey Data Release 9 catalog (Ahn et al. 2012) and transformed to the Johnson system. The magnitudes of the reference stars are listed in Table 1. The final flux-calibrated optical magnitudes of SN 2014cx are shown in Tables 2–4.

2.1.2. *Swift Ultraviolet Observations*

In addition to the ground-based observations, SN 2014cx was also monitored with the Ultraviolet/Optical Telescope

---

[13] IRAF is distributed by the National Optical Astronomy Observatories, which are operated by the Association of Universities for Research in Astronomy, Inc., under cooperative agreement with the National Science Foundation (NSF).

[14] http://sngroup.oapd.inaf.it/snoopy.html

Table 1
Photometric Standard Stars in the Field of SN 2014cx (1σ Uncertainties)

Star ID	α_{J2000} (h m s)	δ_{J2000} (° ′ ″)	*U* (mag)	*B* (mag)	*V* (mag)	*R* (mag)	*I* (mag)
1	1:00:07.08	−7:30:33.54	20.07(09)	19.35(06)	18.31(04)	17.69(05)	17.06(09)
2	0:59:45.87	−7:31:12.11	20.17(11)	19.71(06)	18.66(04)	18.04(04)	17.43(08)
3	0:59:37.53	−7:30:40.79	21.32(25)	20.43(08)	18.79(05)	17.69(11)	16.26(22)
4	0:59:31.84	−7:31:09.63	20.16(10)	19.10(08)	17.56(05)	16.62(07)	15.61(15)
5	0:59:30.89	−7:30:49.81	19.23(06)	18.56(05)	17.58(04)	17.00(04)	16.44(08)
6	0:59:30.53	−7:33:19.29	16.08(03)	17.22(04)	17.29(03)	17.37(04)	17.50(08)
7	1:00:06.41	−7:36:20.14	20.47(15)	19.52(08)	17.96(04)	17.01(07)	16.03(15)
8	1:00:11.55	−7:37:03.82	18.61(04)	18.39(05)	17.56(03)	17.08(04)	16.59(07)
9	1:00:07.93	−7:37:12.15	19.69(08)	19.38(05)	18.45(03)	17.89(04)	17.31(08)
10	1:00:09.75	−7:38:02.37	17.27(03)	17.11(05)	16.28(03)	15.77(04)	15.24(08)
11	1:00:09.58	−7:38:58.23	18.38(04)	18.07(05)	17.19(03)	16.66(04)	16.12(08)
12	0:59:53.05	−7:37:00.70	18.26(04)	18.24(04)	17.52(03)	17.08(03)	16.65(06)
13	0:59:54.59	−7:37:46.63	18.04(04)	17.44(05)	16.47(03)	15.89(04)	15.34(08)
14	0:59:33.31	−7:36:38.75	18.08(09)	17.86(04)	17.12(03)	16.69(03)	16.28(06)
15	0:59:30.12	−7:37:08.94	18.66(10)	18.56(03)	18.20(02)	17.98(03)	17.77(05)

Table 2
Optical Photometry of SN 2014cx from TNT (1σ Uncertainties)

UT Date (yy/mm/dd)	MJD	Phase[a] (day)	*U* (mag)	*B* (mag)	*V* (mag)	*R* (mag)	*I* (mag)
2014 Sep 15	56915.75	13.86	14.30(04)	15.23(03)	14.89(04)	14.70(10)	14.60(05)
2014 Sep 17	56917.75	15.86	⋯	15.14(03)	14.89(07)	14.70(07)	14.56(03)
2014 Oct 12	56942.75	40.86	16.26(08	15.75(01)	⋯	⋯	⋯
2014 Oct 13	56943.75	41.86	16.37(12)	15.87(04)	15.08(04)	14.75(06)	14.46(04)
2014 Oct 21	56951.50	49.61	16.49(06)	15.87(04)	15.01(03)	14.67(04)	14.40(04)
2014 Oct 24	56954.50	52.61	16.57(11)	15.95(03)	15.05(02)	14.78(04)	14.39(04)
2014 Oct 25	56955.50	53.61	16.67(06)	15.98(04)	15.11(02)	14.75(07)	⋯
2014 Oct 26	56956.50	54.61	16.79(05)	16.07(02)	15.11(03)	14.73(05)	⋯
2014 Nov 08	56969.50	67.61	16.87(09)	16.27(03)	15.11(03)	14.77(03)	14.38(04)
2014 Nov 10	56971.50	69.61	17.07(08)	16.27(05)	15.03(03)	14.75(04)	14.44(05)
2014 Nov 11	56972.50	70.61	17.07(05)	16.23(03)	15.06(04)	14.74(04)	14.38(04)
2014 Nov 12	56973.50	71.61	⋯	⋯	15.07(03)	14.78(02)	⋯
2014 Nov 18	56979.50	77.61	17.28(16)	⋯	15.18(05)	14.89(07)	14.40(06)
2014 Nov 19	56980.50	78.61	17.30(15)	16.36(03)	15.15(04)	14.84(05)	14.41(05)
2014 Nov 22	56983.50	81.61	17.46(06)	16.42(05)	15.19(05)	14.82(06)	14.50(04)
2014 Nov 23	56984.50	82.61	17.47(11)	16.34(02)	15.20(04)	14.84(05)	14.51(03)
2014 Nov 24	56985.50	83.61	⋯	⋯	15.22(02)	14.91(03)	14.48(03)
2014 Dec 03	56994.50	92.61	⋯	16.62(04)	15.37(02)	15.03(05)	14.64(02)
2014 Dec 04	56995.50	93.61	⋯	⋯	15.41(02)	15.06(03)	14.59(02)
2014 Dec 05	56996.50	94.61	17.79(25)	16.73(04)	15.45(02)	15.12(03)	14.65(06)
2014 Dec 07	56998.50	96.61	⋯	16.82(05)	15.66(02)	15.18(02)	14.61(04)
2014 Dec 08	56999.50	97.61	17.88(11)	16.94(04)	15.67(06)	15.28(07)	14.74(06)
2014 Dec 16	57007.50	105.61	⋯	17.22(05)	15.82(03)	99.50(05)	14.90(03)
2014 Dec 17	57008.50	106.61	18.03(09)	17.52(06)	16.13(04)	15.46(06)	15.04(04)
2014 Dec 19	57010.50	108.61	⋯	17.27(05)	16.21(04)	15.64(05)	15.23(05)
2014 Dec 20	57011.50	109.61	⋯	17.57(07)	16.10(06)	15.51(05)	15.22(07)
2014 Dec 21	57012.50	110.61	⋯	17.58(05)	16.28(03)	15.68(04)	⋯
2015 Jan 01	57023.50	121.61	⋯	18.04(09)	17.01(06)	16.30(03)	15.92(04)
2015 Jan 03	57025.50	123.61	⋯	18.20(06)	17.02(07)	16.31(05)	15.86(03)
2015 Jan 06	57028.50	126.61	⋯	⋯	⋯	16.31(05)	15.91(05)
2015 Jan 07	57029.50	127.61	⋯	⋯	17.01(04)	16.39(07)	15.89(06)
2015 Jan 08	57030.50	128.61	⋯	18.09(05)	17.21(05)	16.37(05)	15.91(05)
2015 Jan 12	57034.50	132.61	⋯	⋯	⋯	16.34(02)	15.93(04)
2015 Jan 13	57035.50	133.61	⋯	18.23(05)	17.13(04)	16.36(04)	15.95(04)
2015 Jan 18	57040.50	138.61	⋯	⋯	⋯	16.42(03)	16.00(02)
2015 Jan 19	57041.50	139.61	⋯	⋯	17.18(04)	16.41(05)	16.01(05)
2015 Jan 31	57053.50	151.61	⋯	⋯	⋯	16.67(06)	16.20(04)

Note.
[a] Relative to the explosion date, MJD = 56,901.89.

Table 3
Optical Photometry of SN 2014cx from LCOGT (1σ Uncertainties)

UT Date (yy/mm/dd)	MJD	Phase[a] (day)	B (mag)	V (mag)	g (mag)	r (mag)	i (mag)
2014 Sep 03	56903.130	1.240	15.32(03)	15.32(01)	15.23(03)	15.45(02)	15.54(02)
2014 Sep 03	56903.390	1.500	15.34(03)	15.28(03)	15.16(04)	15.36(03)	15.51(02)
2014 Sep 07	56907.770	5.880	15.12(03)	15.01(03)	14.93(03)	14.84(02)	14.92(03)
2014 Sep 12	56912.685	10.795	15.10(03)	14.93(02)	14.96(01)	14.98(03)	14.98(02)
2014 Sep 14	56914.755	12.865	15.20(03)	14.92(03)	15.07(03)	14.95(03)	14.92(04)
2014 Sep 16	56916.690	14.800	⋯	⋯	15.00(02)	14.82(02)	14.93(03)
2014 Sep 18	56918.685	16.795	15.25(04)	14.94(05)	15.03(03)	14.81(02)	14.92(07)
2014 Sep 20	56920.545	18.655	15.30(02)	14.91(02)	⋯	14.79(03)	14.88(07)
2014 Sep 23	56923.540	21.650	15.29(02)	14.88(03)	15.04(04)	14.76(03)	14.94(05)
2014 Sep 27	56927.545	25.655	15.45(03)	14.92(02)	15.12(03)	14.76(03)	14.82(04)
2014 Sep 29	56929.395	27.505	15.48(03)	14.94(03)	⋯	⋯	⋯
2014 Oct 02	56932.520	30.630	15.58(03)	14.94(02)	15.20(01)	14.76(01)	14.81(05)
2014 Oct 03	56933.715	31.825	15.56(03)	14.97(03)	15.29(04)	14.78(02)	14.79(03)
2014 Oct 09	56939.690	37.800	15.73(04)	15.01(03)	15.34(05)	14.87(03)	14.80(02)
2014 Oct 13	56943.830	41.940	15.80(02)	15.03(02)	15.39(03)	14.80(02)	14.85(02)
2014 Oct 17	56947.475	45.585	15.86(03)	15.06(02)	15.40(01)	14.80(02)	14.79(02)
2014 Oct 21	56951.565	49.675	⋯	⋯	15.42(02)	14.87(02)	14.74(02)
2014 Oct 25	56955.405	53.515	15.94(04)	15.12(04)	15.47(03)	14.76(04)	14.80(03)
2014 Nov 01	56962.565	60.675	16.06(03)	15.07(03)	15.55(03)	14.83(03)	14.77(03)
2014 Nov 06	56967.980	66.090	16.13(02)	15.10(03)	15.54(03)	14.82(03)	14.79(03)
2014 Nov 13	56974.630	72.740	16.26(03)	15.16(03)	15.63(04)	14.94(04)	14.85(05)
2014 Nov 18	56979.900	78.010	16.30(03)	15.16(02)	15.68(03)	14.89(02)	14.88(03)
2014 Nov 25	56986.060	84.170	16.43(03)	15.26(02)	15.80(04)	14.99(03)	14.89(03)
2014 Nov 27	56988.890	87.000	16.41(03)	15.25(03)	⋯	⋯	⋯
2014 Nov 28	56989.780	87.890	16.49(04)	15.32(03)	15.83(02)	14.99(02)	14.97(03)
2014 Dec 04	56995.820	93.930	16.65(04)	15.44(02)	15.96(04)	15.08(03)	15.00(02)
2014 Dec 04	56995.850	93.960	16.71(04)	15.47(03)	⋯	⋯	⋯
2014 Dec 09	57000.120	98.230	17.04(05)	15.57(02)	16.15(04)	15.33(03)	15.11(04)
2014 Dec 12	57003.830	101.940	16.95(04)	15.67(02)	16.24(03)	15.33(02)	15.24(05)
2014 Dec 16	57007.545	105.655	17.26(05)	15.92(03)	16.56(04)	15.51(03)	15.46(02)
2014 Dec 20	57011.480	109.590	17.63(04)	16.25(02)	16.84(03)	15.74(02)	15.67(05)
2014 Dec 24	57015.425	113.535	17.84(06)	16.60(03)	17.18(04)	16.03(01)	15.92(03)
2014 Dec 30	57021.430	119.540	18.09(07)	17.04(04)	17.53(05)	16.44(03)	16.44(09)
2015 Jan 02	57024.485	122.595	⋯	⋯	17.55(06)	16.48(05)	16.47(06)
2015 Jan 03	57025.795	123.905	18.16(05)	17.04(03)	17.59(04)	16.48(03)	16.43(05)
2015 Jan 05	57027.830	125.940	18.22(05)	17.14(03)	17.66(05)	16.51(02)	16.54(03)
2015 Jan 08	57030.445	128.555	18.36(05)	17.21(04)	17.76(04)	16.59(03)	16.58(03)
2015 Jan 09	57031.815	129.925	18.33(05)	17.19(03)	⋯	⋯	⋯
2015 Jan 10	57032.060	130.170	18.31(05)	17.15(03)	⋯	⋯	⋯
2015 Jan 11	57033.795	131.905	18.37(05)	17.28(02)	17.66(03)	16.64(02)	16.58(02)
2015 Jan 14	57036.070	134.180	18.35(05)	17.23(03)	17.69(04)	16.63(03)	16.61(04)
2015 Jan 15	57037.445	135.555	⋯	⋯	17.81(04)	16.58(03)	16.62(03)
2015 Jan 16	57038.790	136.900	18.40(07)	17.23(04)	17.74(04)	16.62(03)	16.64(03)
2015 Jan 22	57044.790	142.900	⋯	17.24(03)	17.76(04)	16.71(05)	16.65(05)
2015 Jan 28	57050.085	148.195	18.44(07)	17.32(04)	17.86(05)	16.69(03)	16.76(05)
2015 Jan 29	57051.080	149.190	18.41(08)	17.33(04)	17.93(06)	16.72(03)	16.82(05)
2015 Feb 11	57064.775	162.885	18.49(08)	17.52(04)	17.91(04)	16.79(03)	16.85(04)
2015 Feb 20	57073.075	171.185	18.45(08)	17.57(04)	⋯	⋯	⋯
2015 Jun 04	57177.420	275.530	⋯	⋯	⋯	17.81(04)	18.06(10)
2015 Jun 22	57195.790	293.900	⋯	⋯	⋯	18.03(09)	18.02(06)
2015 Jun 30	57203.395	301.505	18.92(05)	18.44(05)	18.65(04)	17.85(04)	18.206(04)
2015 Jul 17	57220.260	318.370	18.93(05)	18.52(04)	18.69(07)	18.11(06)	18.200(06)
2015 Aug 13	57247.330	345.440	⋯	⋯	18.70(05)	18.36(05)	18.259(04)
2015 Aug 29	57263.255	361.365	⋯	⋯	19.02(21)	18.27(23)	⋯
2015 Sep 17	57282.390	380.500	⋯	⋯	19.03(05)	18.50(05)	18.198(05)

Note.
[a] Relative to the explosion date, MJD = 56,901.89.

(UVOT; Roming et al. 2005) on board the *Swift* spacecraft through the *uvw*2, *uvm*2, *uvw*1, *u*, *b*, and *v* filters. The UV observations began on 2014 September 3 and ended on 2014 October 24. The data were obtained from the *Swift* Optical/Ultraviolet Supernova Archive (Brown et al. 2014). The reduction method for UVOT photometry is

Table 4
Unfiltered Photometry of SN 2014cx (1σ Uncertainties)

MJD	Phase[a]	Mag	Error	Telescope	MJD	Phase[a]	Mag	Error	Telescope
56871.49	−30.40	>18.76	⋯	KAIT	56949.38	47.49	14.87	0.08	KAIT
56876.49	−25.40	>19.16	⋯	KAIT	56950.31	48.42	14.73	0.12	KAIT
56877.48	−24.41	>19.06	⋯	KAIT	56952.31	50.42	14.78	0.06	KAIT
56879.41	−22.48	>18.50	⋯	KAIT	56954.33	52.44	14.79	0.05	KAIT
56880.41	−21.48	>18.67	⋯	KAIT	56957.31	55.42	14.86	0.05	KAIT
56881.39	−20.50	>18.38	⋯	KAIT	56958.33	56.44	14.84	0.05	KAIT
56886.46	−15.43	>19.48	⋯	KAIT	56959.28	57.39	14.80	0.07	KAIT
56887.47	−14.42	>19.05	⋯	KAIT	56960.26	58.37	14.88	0.06	KAIT
56888.45	−13.44	>19.22	⋯	KAIT	56964.29	62.40	14.90	0.07	KAIT
56889.45	−12.44	>19.14	⋯	KAIT	56970.32	68.43	14.80	0.09	KAIT
56890.45	−11.44	>19.13	⋯	KAIT	56971.26	69.37	14.86	0.07	KAIT
56891.44	−10.45	>19.14	⋯	KAIT	56972.26	70.37	14.80	0.06	KAIT
56892.47	−9.42	>19.26	⋯	KAIT	56976.32	74.43	14.90	0.07	KAIT
56893.41	−8.48	>19.15	⋯	KAIT	56977.25	75.36	14.85	0.06	KAIT
56894.48	−7.41	>18.88	⋯	KAIT	56978.25	76.36	14.85	0.12	KAIT
56895.42	−6.47	>19.17	⋯	KAIT	56985.23	83.34	14.89	0.08	KAIT
56896.41	−5.48	>19.22	⋯	KAIT	56986.24	84.35	14.96	0.06	KAIT
56897.49	−4.40	>19.14	⋯	KAIT	56987.23	85.34	15.09	0.05	KAIT
56898.40	−3.49	>19.13	⋯	KAIT	56988.26	86.37	15.11	0.08	KAIT
56900.40	−1.49	>19.19	⋯	KAIT	56989.19	87.30	14.99	0.06	KAIT
56901.39	−0.50	>19.11	⋯	KAIT	56990.18	88.29	15.07	0.05	KAIT
56902.40	0.51	15.69	0.05	KAIT	56999.24	97.35	15.27	0.07	KAIT
56903.36	1.47	15.17	0.07	KAIT	57001.22	99.33	15.28	0.08	KAIT
56920.41	18.52	14.85	0.06	KAIT	57006.14	104.25	15.47	0.09	KAIT
56922.33	20.44	14.65	0.06	KAIT	57015.12	113.23	16.05	0.07	KAIT
56923.30	21.41	14.67	0.08	KAIT	57027.08	125.19	16.54	0.15	KAIT
56924.30	22.41	14.65	0.05	KAIT	56902.57	0.68	15.6	⋯	Koichi Itagaki
56944.36	42.47	14.70	0.07	KAIT	56903.04	1.15	15.2	⋯	T. Yusa
56946.35	44.46	14.83	0.11	KAIT	56906.93	5.04	14.8	⋯	Paolo Campaner

Note.
[a] Relative to the explosion date, MJD = 56,901.89.

Table 5
UV and Optical Photometry of SN 2014cx from *Swift* (1σ Uncertainties)

UT Date (yy/mm/dd)	MJD	Phase[a] (day)	*uvw*2 (mag)	*uvm*2 (mag)	*uvw*1 (mag)	*U* (mag)	*B* (mag)	*V* (mag)
2014 Sep 3	56903.03	1.14	13.62(05)	13.70(05)	13.80(05)	13.95(04)	15.34(06)	15.42(07)
2014 Sep 4	56904.62	2.73	13.70(05)	13.67(05)	13.66(05)	13.74(04)	14.97(05)	15.09(06)
2014 Sep 5	56905.26	3.37	13.86(05)	13.71(05)	13.77(05)	13.78(04)	14.95(05)	15.09(06)
2014 Sep 6	56906.09	4.20	14.06(05)	13.85(05)	13.80(05)	13.78(04)	14.96(05)	15.01(06)
2014 Sep 7	56907.25	5.36	14.32(06)	14.03(06)	13.92(05)	13.78(04)	14.92(05)	15.00(06)
2014 Sep 8	56908.31	6.42	14.54(07)	⋯	14.00(05)	13.80(04)	14.88(05)	⋯
2014 Sep 9	56909.09	7.20	14.80(07)	14.40(06)	14.11(05)	13.83(04)	14.92(05)	14.97(06)
2014 Sep 12	56912.91	11.02	15.48(09)	15.19(08)	14.60(06)	13.99(04)	14.90(05)	14.97(06)
2014 Sep 16	56916.28	14.39	16.22(11)	16.25(10)	15.30(08)	14.24(05)	15.02(05)	14.99(06)
2014 Sep 20	56920.78	18.89	17.67(24)	17.80(24)	16.32(11)	14.62(05)	15.25(06)	14.96(06)
2014 Sep 24	56924.71	22.82	18.21(36)	18.37(42)	16.82(15)	15.28(07)	15.35(06)	14.94(06)
2014 Sep 28	56928.60	26.71	18.55(46)	⋯	17.51(21)	15.62(07)	15.45(06)	14.96(06)
2014 Oct 4	56934.23	32.34	⋯	⋯	18.08(30)	15.85(07)	15.62(06)	14.95(07)
2014 Oct 11	56941.27	39.38	⋯	⋯	⋯	16.22(07)	15.80(06)	15.08(06)
2014 Oct 19	56949.91	48.02	⋯	⋯	18.62(47)	16.46(07)	16.00(06)	15.12(06)
2014 Oct 22	56952.70	50.81	⋯	⋯	⋯	16.39(14)	15.96(09)	15.06(09)
2014 Oct 24	56954.60	52.71	⋯	⋯	⋯	16.56(07)	16.01(06)	15.09(06)

Note.
[a] Relative to the explosion date, MJD = 56,901.89.

based on that of Brown et al. (2009), which includes aperture photometry after subtracting off the underlying galaxy count rates, and adopting the updated zeropoints and time-dependent sensitivity from Breeveld et al. (2011). The final UVOT photometry of SN 2014cx is presented in Table 5.

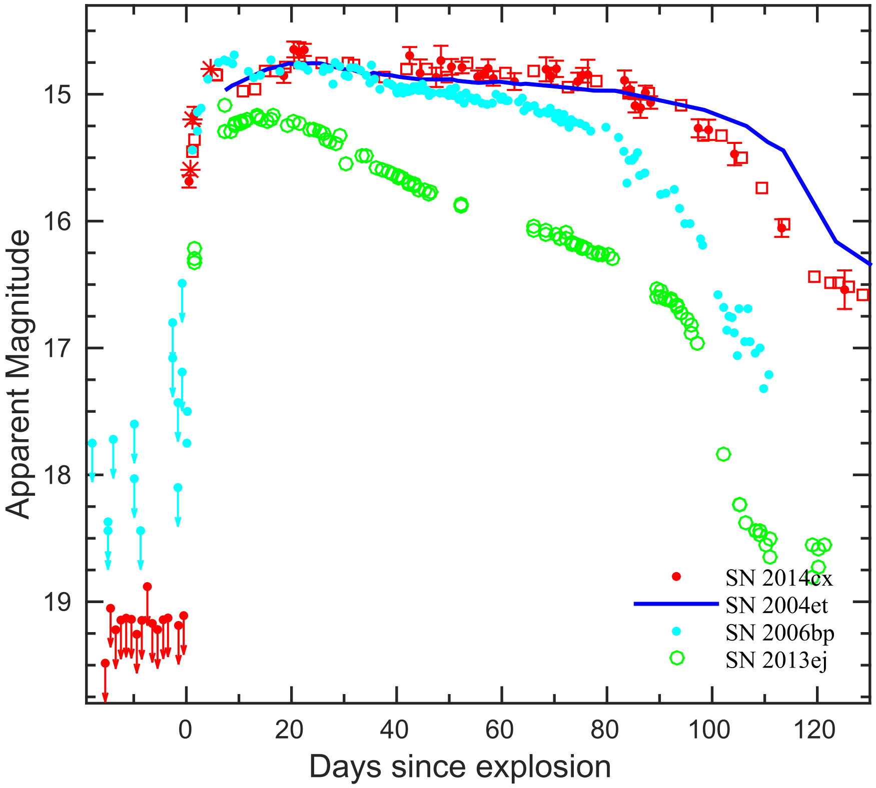

Figure 2. KAIT unfiltered (red circle) and LCOGT *r*-band (red square) light curve of SN 2014cx unfiltered detections from the *Bright Supernovae* website (http://www.rochesterastronomy.org/snimages/; red star), SN 2004et in the *R* band (blue line), SN 2006bp (cyan), and SN 2013ej (green). For KAIT data, detections are plotted with filled circles, and arrows represent 4σ upper limits.

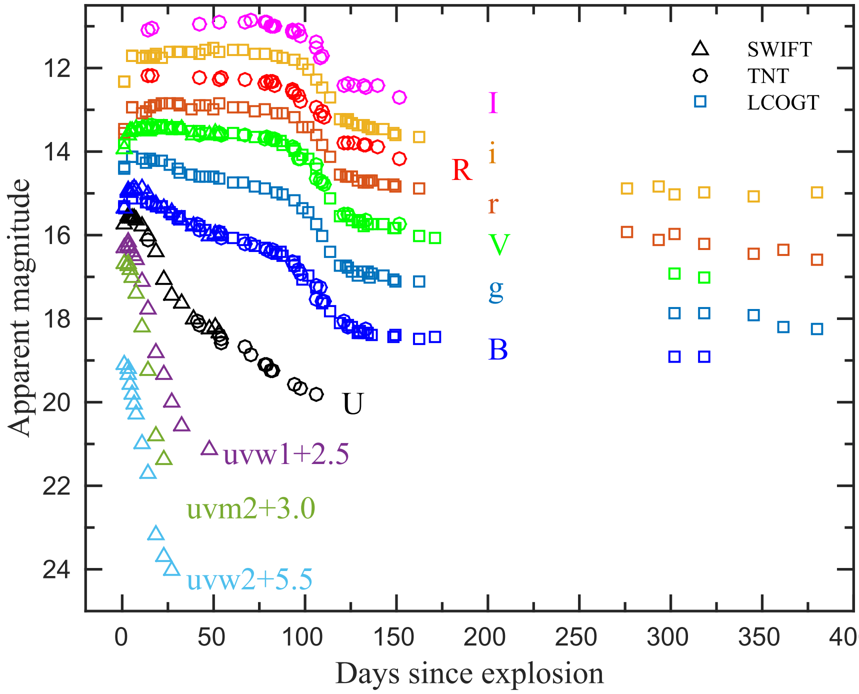

Figure 3. Photometric evolution of SN 2014cx in UV and optical bands. The phase is given relative to the estimated explosion date, MJD = 56,901.89.

2.2. Spectroscopy

The spectroscopic monitoring campaign of SN 2014cx started on 2014 September 7 and continued for ~400 days. Fourteen low-resolution optical spectra were obtained using the LCOGT 2 m Faulkes Telescope South (FTS; with FLOYDS), the Xinglong 2.16 m telescope (with BFOSC), the Lijiang 2.4 m telescope (with YFOSC), the LCOGT 2 m Faulkes Telescope North (FTN; with FLOYDS), the GEMINI-North

Telescope (GNT; with GMOS), and the Keck I 10 m telescope (with LRIS); see Table 7 for the detailed information on the spectroscopic observations.

The spectra were all reduced in a standard manner using various tasks within IRAF. After the preliminary reduction (including bias/overscan correction, flat fielding, and cosmic-ray removal), the one-dimensional spectra were extracted using the optimal extraction method (Horne 1986). Wavelengths of the SN spectra were calibrated using the Fe/Ar and Fe/Ne lamp spectra. For the FLOYDS spectra, a Hg/Ar lamp is used for wavelength calibration. The spectra were then flux calibrated using the instrumental sensitivity curves of spectrophotometric standard stars observed on the same (or nearby) night and with the same instrumental setup.

3. PHOTOMETRIC ANALYSIS

3.1. The Early Time Evolution

With modern high-cadence surveys, we are able to detect young SNe and trigger follow-up observations immediately. Such early time detections help constrain the explosion properties and (with luck) even reveal shock breakout, which often happens hours after explosion (Quimby et al. 2007; Schawinski et al. 2008; Tominaga et al. 2009; Gezari et al. 2015; Dhungana et al. 2016; Garnavich et al. 2016).

The field of SN 2014cx was monitored daily by KAIT in the clear band (i.e., unfiltered) before the explosion, leading to the earliest detection of this object after the explosion. Figure 2 shows the KAIT unfiltered light curve, spanning from a few weeks before the explosion to ∼120 days after. A few early time observations obtained by amateurs in unfiltered mode are also overplotted. As can be seen, SN 2014cx was not detected on 2014 September 1 (MJD = 56,901.39) with a limit of >19.1 mag, but it was detected one day later (MJD = 56,902.40) at 15.69 mag. We therefore adopt this epoch (MJD = 56901.89 ± 0.5) as the reference date for the shock breakout for SN 2014cx, and this determination sets one of the tightest constraints on the shock breakout time for a SN IIP based on the observations of ground-based telescopes.

The unfiltered light curve of SN 2014cx at early time (0–20 days) is very similar to those of SN 2006bp and SN 2013ej. It seems to experience three stages. First, the SN brightened by more than 4 mag over the first 1.5–2.0 days, and it then dimmed and rebrightened toward the primary peak at $t \approx 20$ days. This trend is actually more prominent in the early time evolution of the LCOGT r-band light curve (see Figure 2), with a noticeable dip occurring at $t \approx 10$ days after explosion. Such a behavior is also seen in the comparison object SN 2006bp (and possibly SN 2013ej), which is likely related to the shock breakout of the supernova surface and its cooling phase (Quimby et al. 2007).

3.2. Overall Evolution of the Light Curves

Figure 3 shows the multicolor photometric evolution of SN 2014cx during the period from $t = +1$ to $t = +380$ days after the explosion. At the earliest phases, the light curves exhibit a rapid rise in the UV and optical bands, but with a slower pace at longer wavelengths (see Table 6). By fitting a low-order polynomial to the data around maximum light, we determine the magnitudes and corresponding dates at peak brightness. These results are also presented in Table 6. We note that the rise time in the B band is ∼8 days, which agrees well with the statistical result from a large sample of SNe II (González-Gaitán et al. 2015).

One can see from Figure 3 that the UV light curves show rapid post-peak declines, with slopes of 0.16, 0.23, and 0.25 mag day^{-1} in the $uvw1$, $uvw2$, and $uvm2$ bands, respectively. The optical light curves, in contrast, drop slowly and settle to the plateau phase. A decline rate of $\beta_{100}^{B} = 2.5$ mag is

Table 6
Photometric Parameters of SN 2014cx

	U	B	V	R	I
Peak magnitude	13.75	15.08	14.91	⋯	⋯
Phase of maximum[a]	3.29	8.24	10.83	⋯	⋯
Plateau magnitude	⋯	⋯	15.10	14.75	14.38
Decay rate (mag/100 day)	⋯	0.42	0.95	1.09	1.13

Note.
[a] Relative to the explosion date, MJD = 56,901.89.

Table 7
Observing Log for Optical Spectra of SN 2014cx

UT Date	MJD	Phase[a] (days)	Range (Å)	Exposure (s)	Telescope + Instrument
2014 Sep 7	56907.74	5.8	3400–8500	2700	LCOGT 2.0 m Telescope South + FLOYDS
2014 Sep 12	56912.69	10.8	3400–8500	1800	LCOGT 2.0 m Telescope South + FLOYDS
2014 Sep 18	56918.66	16.8	3480–8850	2100	Xinglong 2.16 m + BFOSC
2014 Sep 22	56922.46	20.6	3400–9000	1800	LCOGT 2.0 m Telescope South + FLOYDS
2014 Sep 26	56926.71	24.8	3400–10,000	1800	LCOGT 2.0 m Telescope South + FLOYDS
2014 Sep 29	56929.65	27.8	3400–10,000	1800	LCOGT 2.0 m Telescope South + FLOYDS
2014 Oct 3	56933.70	31.8	3400–10,000	2700	LCOGT 2.0 m Telescope South + FLOYDS
2014 Oct 12	56942.46	40.6	3400–10,000	2700	LCOGT 2.0 m Telescope South + FLOYDS
2014 Oct 16	56946.60	44.6	3500–9000	2100	Lijiang 2.4 m + YFOSC
2014 Oct 21	56951.65	49.8	3400–10,000	2700	LCOGT 2.0 m Telescope South + FLOYDS
2014 Dec 7	56998.36	96.5	3400–10,000	2700	LCOGT 2.0 m Telescope North + FLOYDS
2015 Jan 8	57030.43	128.6	3900–8800	2400	Xinglong 2.16 m + BFOSC
2015 Jul 27	57230.62	328.7	3900–9700	900	Gemini-North 8.1 m + GMOS
2015 Oct 10	57305.38	403.5	3800–10,000	1200	Keck I 10 m + LRIS

Note.
[a] Relative to the explosion date, MJD = 56,901.89.

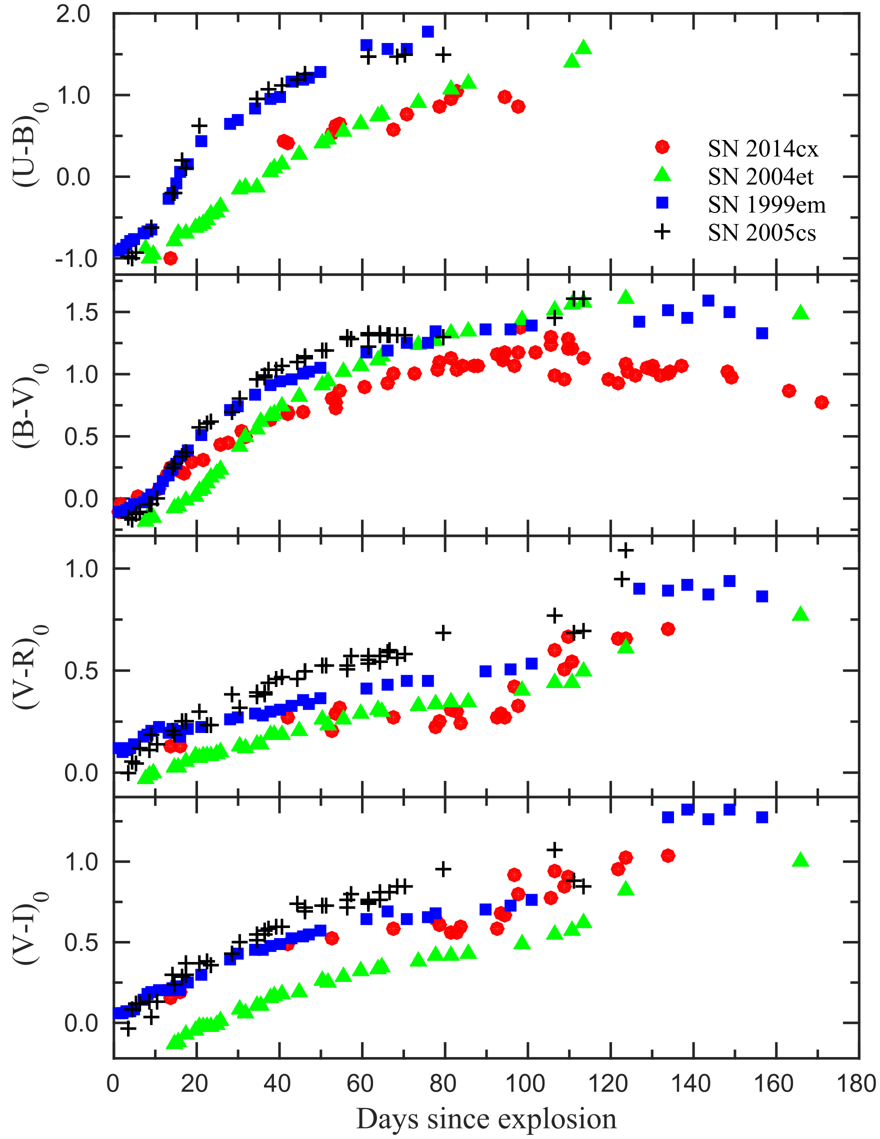

Figure 4. Dereddening optical color evolution of SN 2014cx compared with those of other SNe IIP : SNe 1999em, 2004et, and 2005cs.

measured for the *B*-band light curve over the first 100 days after maximum light, consistent with the typical value obtained for normal SNe IIP (i.e., $\beta^B_{100} < 3.5$ mag; Patat et al. 1994). The *V*-band brightness declines by ~0.2 mag in the first 50 days after the peak, which also falls into the SN IIP group according to the criterion of Faran et al. (2014b). For SN 2014cx, the plateau phase lasts for ~100 days, and its brightness stays roughly constant, especially in the *VrRiI* bands.

After the plateau, the SN 2014cx experiences a sudden drop in brightness in all optical bands, with magnitude declines of 1.5–2.0 mag in ~20 days. To derive the parameters about the transitional phase, we fit the *V*-band light curve using Equation (4) from Olivares et al. (2010). The middle date of the transition phase, $t_{\rm PT}$, is found to be ~109 days, and the width of the transition phase is ~7 days. During the tail phase (i.e., $t \approx 130$–170 days), the decline rates in *B*, *V*, *R*, and *I* are measured to be 0.42, 0.95, 1.09, and 1.13 mag $(100\ {\rm day})^{-1}$, respectively. These values are similar to those of normal SNe IIP such as SN 1999em (Elmhamdi et al. 2003). In the *V* and *R* bands, the decline rates are found to be comparable to the values expected for the radioactive decay, 0.98 mag $(100\ {\rm day})^{-1}$ (Patat et al. 1994). This indicates that the gamma-ray photons were effectively trapped in the ejecta at this phase. After $t \approx 170$ days, the light curves tend to show slower decline rates relative to the earlier nebular phase. For example, the decline rate of *B*- and *V*-band light curve is measured to be 0.32 and 0.65 mag $(100\ {\rm day})^{-1}$ during the period from 170 days $< t <$ 320 days. And this decay rate is found to be 0.46, 0.85, and 0.81 mag $(100\ {\rm day})^{-1}$ in *gri* bands at similar phase. This slower evolution can be due to interaction of SN ejecta with the circumstellar materials (CSM) surrounding the SN or a scattered-light echo (see discussions in Section 4.1).

3.3. Color Curves

The Galactic reddening in the direction of NGC 337 is $E(B-V)_{\rm MW} = 0.10$ mag (Schlafly & Finkbeiner 2011). We did not detect any significant features of Na I D absorption produced by the host galaxy in our 14 low-resolution spectra, suggesting that host-galaxy reddening might be negligible for SN 2014cx. As an alternative, we also use the color method proposed by Olivares et al. (2010) to estimate the reddening

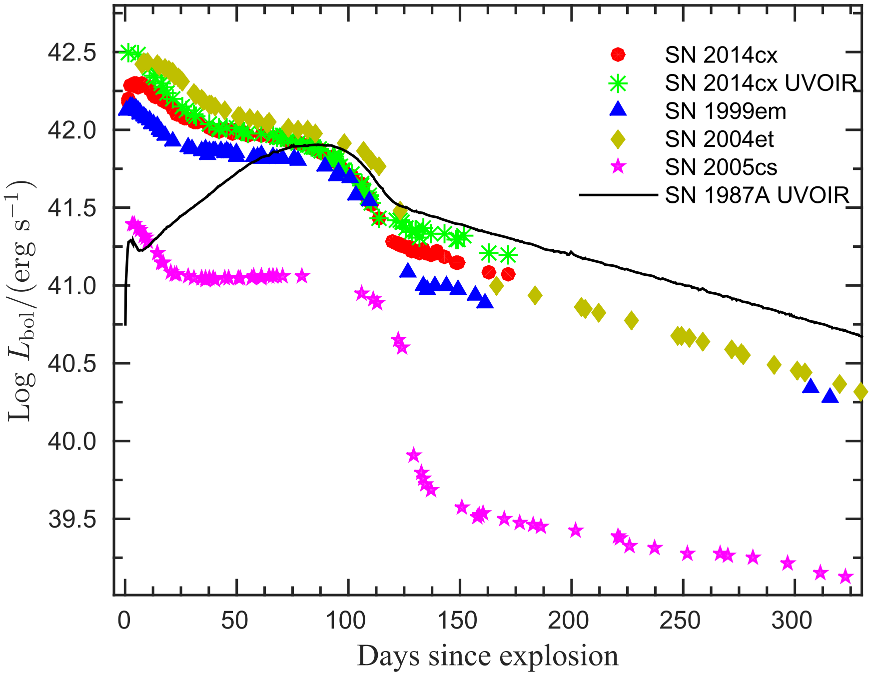

Figure 5. Comparison of the bolometric luminosity evolution of SN 2014cx and other well-studied SNe IIP.

due to the host galaxy. This method assumes that the intrinsic $V-I$ color of SNe IIP is constant (i.e., $(V-I)_0 = 0.656$ mag) toward the end of the plateau. After correcting for the Galactic reddening, the $V-I$ color of SN 2014cx is found to be 0.596 mag at $t = 79$ days, which gives a negative host-galaxy extinction for this object. Thus, we adopt $E(B-V)_{\rm tot} = 0.10$ mag in the following analysis, which corresponds to a total line-of-sight extinction of $A_V = 0.31$ mag assuming the ratio of total to selective extinction $R_V = 3.1$ (Cardelli et al. 1989).

The reddening-corrected $(U-B)_0$, $(B-V)_0$, $(V-R)_0$, and $(V-I)_0$ color curves of SN 2014cx are shown in Figure 4. For comparison, we overplot the dereddened color curves of three well-studied Type IIP SNe 1999em, 2004et, and 2005cs. The color evolution of SN 2014cx follows the general trend seen in SNe IIP: a rapid decrease from blue (high temperature) to red (low temperature) during the photospheric phase. The $(U-B)_0$ and $(B-V)_0$ colors become redder by ~1–2 mag in the first 100 days, while the $(V-R)_0$ and $(V-I)_0$ colors evolve slowly and become red by only ~0.5 mag. The $(B-V)_0$ color turns blue after t ~120 days, when the nebular phase begins. The overall colors of SN 2014cx are bluer than those of SN 1999em at all phases, except in $V-I$ where these two objects have similar colors. This suggests that SN 2014cx has a higher photospheric temperature than SN 1999em.

3.4. Bolometric Light Curve

To derive the bolometric luminosity of SN 2014cx, we first convert the extinction-corrected magnitudes in different bands to flux values at the effective wavelength, and then integrate the combined flux over wavelength. The luminosity can then be calculated using the integrated flux and a distance of 18 Mpc (see Section 2). During the first 50 days, when *Swift* UV photometry was available, we integrated the UV flux and extrapolated it to the optical flux. As the UV flux decreases quickly, we assume that the UV contribution to the bolometric flux is marginal in the late plateau phase and negligible ($\lesssim$1%) during the nebular phase (e.g., Dall'Ora et al. 2014). Owing to the lack of NIR data, we estimate the tail luminosity using Equation (3) in Maguire et al. (2010), where a bolometric correction of 0.33 ± 0.06 mag is adopted.

Figure 5 shows the UV–optical–NIR ("UVOIR") bolometric luminosity curve of SN 2014cx. One can see that it reached a peak of $\log\,[L_{\rm bol}^{\rm peak}/({\rm erg\ s^{-1}})] = 42.47$ at ~3 days after explosion. In Figure 5 we also compare the *UBVRI* quasi-bolometric luminosity of SN 2014cx with that of some well-studied SNe IIP. It is readily seen that the luminosity evolution of SN 2014cx is similar to that of SN 2004et and SN 1999em but lies between these two objects in the early and plateau phases. In the nebular phase, we note that the tail luminosity of SN 2014cx is apparently higher than SN 1999em and even slightly higher than SN 2004et, suggesting that a relatively larger amount of nickel may be synthesized in its explosion (see discussion below).

3.5. ^{56}Ni Mass

For SNe IIP, the light curve in the nebular phase is powered mainly by the radioactive decay chain $^{56}{\rm Ni} \rightarrow {}^{56}{\rm Co} \rightarrow {}^{56}{\rm Fe}$. And the tail luminosity is directly proportional to the mass of synthesized ^{56}Ni supposing that the gamma-ray deposition fraction is similar. For the well-studied Type II-pec SN 1987A, the mass of ^{56}Ni has been determined to be $0.075 \pm 0.005\,M_\odot$ (Arnett 1996). For SN 2014cx we estimate the UVOIR bolometric luminosity at $t \approx 150$ days to be $1.93 \pm 0.14 \times 10^{41}$ erg s^{-1} by making a linear fit to the evolution between $t \approx 120$ days and $t \approx 200$ days. The luminosity of SN 1987A at the same phase is estimated to be $2.47 \pm 0.02 \times 10^{41}$ erg s^{-1}. The ratio of SN 2014cx to SN 1987A is 0.78 ± 0.06, which yields a value of $M_{\rm Ni} = 0.058 \pm 0.006\,M_\odot$ for SN 2014cx.

Based on the assumption that all γ-rays from $^{56}{\rm Co} \rightarrow {}^{56}{\rm Fe}$ are entirely thermalized, Hamuy (2003) found an independent

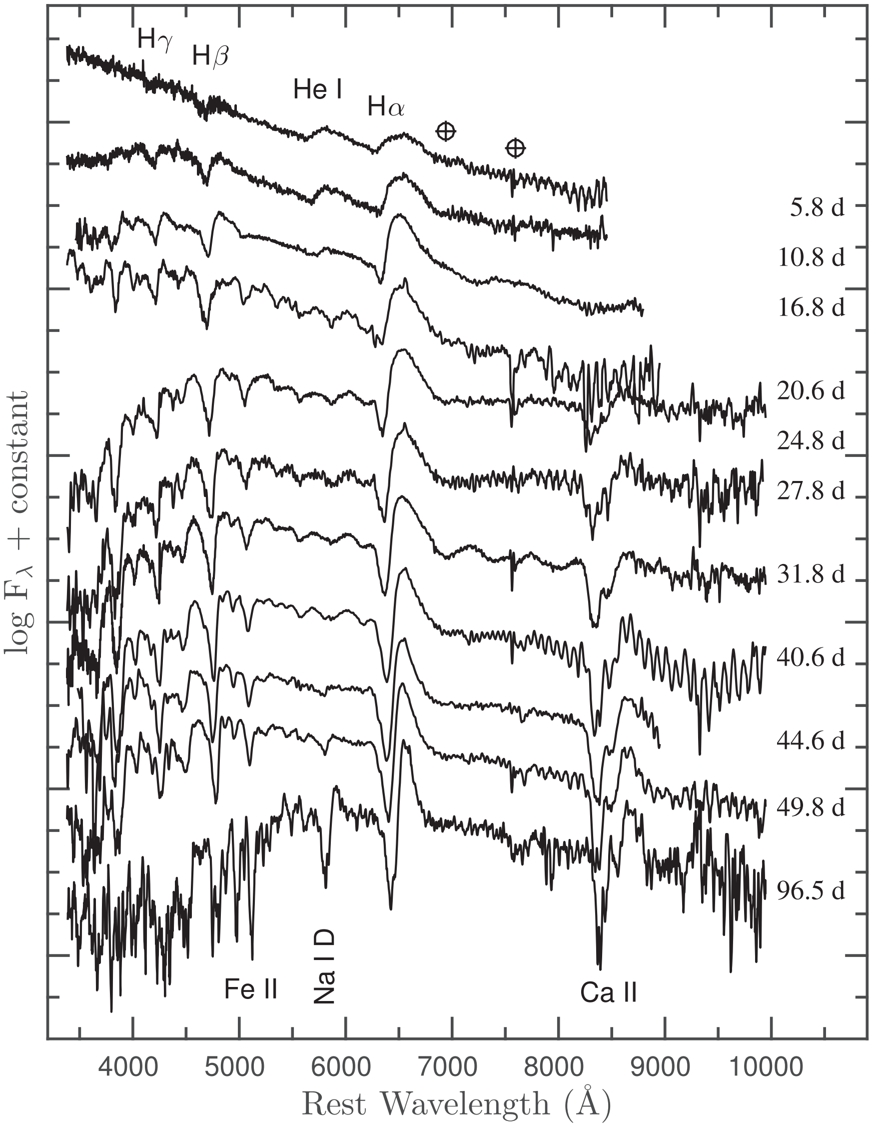

Figure 6. Spectroscopic evolution of SN 2014cx during the photospheric phase. The spectra have been corrected for the redshift of the host galaxy NGC 337 ($z = 0.00549$, via NED). Some key features are labeled, as are residuals from telluric absorption lines. The oscillations in some of the near-infrared spectra (most notably, at 40.6 day) are caused by incomplete removal of CCD fringing.

relationship to estimate the value of ^{56}Ni mass using the tail luminosity (L_t). We calculated L_t of SN 2014cx at 17 epochs from $t \approx 120$ days to ≈ 170 days using the late time V-band magnitude. The mean value of $M_{\rm Ni}$ resulting from Equation (2) of Hamuy (2003) is $0.055 \pm 0.011\ M_\odot$, consistent with the result from direct comparison with SN 1987A.

Following the procedures of Elmhamdi et al. (2003), we also estimated the ^{56}Ni mass using the steepness parameter S, which is defined as the steepest value in the V-band light curve at the transitional phase from plateau to nebular tail. For SN 2014cx, we obtain $S = 0.071$ mag day^{-1} and $M_{\rm Ni} = 0.056 \pm 0.007\ M_\odot$, in good agreement with the values derived from the observed luminosity in the radioactive tail. The weighted mean value of $M_{\rm Ni}$ derived from above three results is $0.056 \pm 0.008\ M_\odot$.

4. SPECTROSCOPIC ANALYSIS

4.1. Optical Spectra

The overall spectroscopic evolution of SN 2014cx is displayed in Figures 6 and 7, covering early time ($\sim +6$ day) up to the nebular phase ($\sim +404$ day). All of the spectra have been corrected for the recession velocity of the host galaxy (1646 km s^{-1}) but not for the reddening. The main spectral features are labeled according to the lines previously identified for SNe IIP (Leonard et al. 2002).

At $t \approx 6$ days, the spectrum is very blue with a blackbody temperature exceeding 10^4 K. The prominent features at such early phases are Balmer lines and He I λ5876 with broad P-Cygni profiles. At $t \approx 17$ days, the Fe II λ5169 absorption feature is visible, and it becomes stronger by $t \approx 21$ days along with Fe II λ5018. The Na I and He I lines are also detectable at $t \approx 21$ days, and both features grow stronger thereafter. The continuum becomes notably redder from $t \approx 21$ days to $t \approx 25$ days, suggesting a rapid decrease of the photospheric temperature during this period. Consequently, more metal lines (such as Sc II, Ba II, O I, and the Ca II NIR triplet) are formed, and they gradually become the dominant features in the spectra.

At $t \approx 128$ days, SN 2014cx starts to enter the nebular phase. The spectrum shows deep absorption of Na I and prominent emission lines of [O I] λλ6300, 6364, [Fe II] λλ7155, and [Ca II]

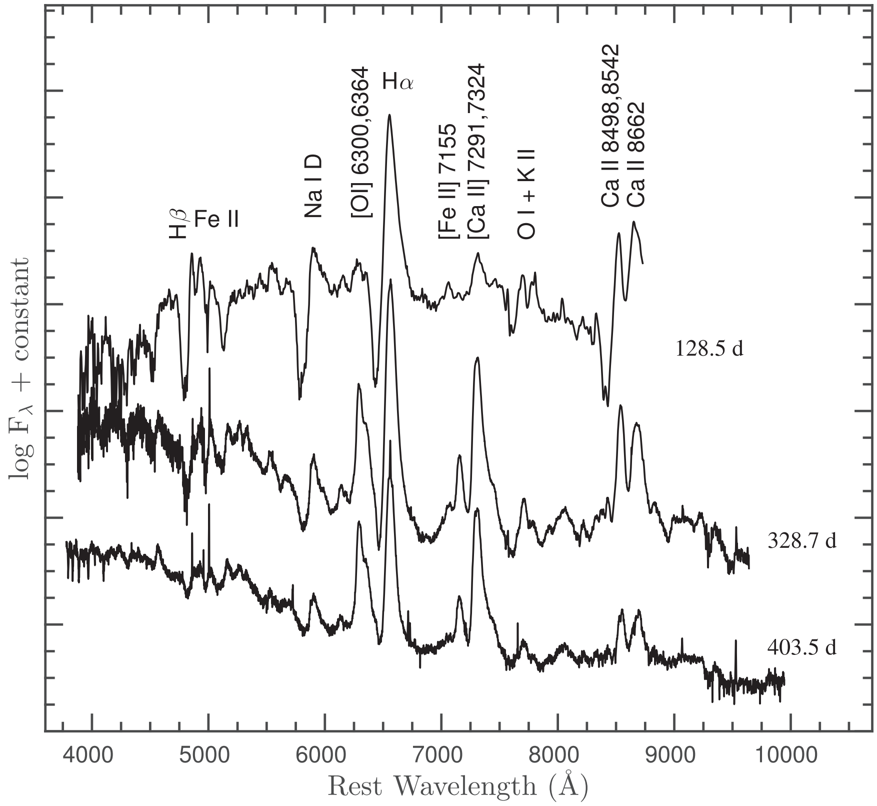

Figure 7. Spectroscopic evolution of SN 2014cx during the nebular phase, when emission lines are dominant features.

$\lambda\lambda$7291, 7324. At $t \approx 329$ days and $t \approx 404$ days, the spectra exhibit emission lines of Hα, [O I], [Fe II], and [Ca II], as well as P-Cygni profiles of Na I, O I, Fe II, and the Ca II NIR triplet. The multiple emission peaks at 5000–5500 Å are likely contributed by [Fe I] and [Fe II] multiplets. We note that the continuum at 3800–5000 Å is relatively bluer than that taken at 128 days perhaps because of either a scattered-light echo off the surrounding CSM (Andrews et al. 2016) or late time CSM interaction (Inserra et al. 2011). For the light-echo scenario, the echoed light should come from earlier phases when the spectra were blue, and the scattering is more efficient at shorter wavelengths. However, the negligible extinction estimated for SN 2014cx in Section 3.3 implies that the CSM potentially causing the light echoes is in the opposite direction of SN 2014cx. In the case of the CSM interaction, we can also see a hint of narrow Hα emission in the spectrum at $t \approx 404$ days.

In Figure 8, we compare the spectra of SN 2014cx at about one week, 50 days, and one year after explosion with those of SN 1999em, SN 2005cs, and SN 2004et at similar phases. It can be seen that SN 2014cx has relatively shallower line profiles than the comparison SNe at early phases. During the plateau phase, $t \approx 50$ days after the explosion, the hydrogen lines of SN 2014cx are similar to those of the comparison SNe IIP, but stronger than those of the subluminous SN 2005cs. In the nebular phase ($t \approx 300$ days), however, SN 2014cx appears to have weaker spectral features than SN 1999em and SN 2004et, but stronger than SN 2005cs, consistent with a flux contribution to the continuum.

4.2. Expansion Velocities

We measured the relativistic Doppler velocities of the Hα, Hβ, Fe II λ5169, and Sc II λ6245 lines during the photospheric phase by fitting a Gaussian function to their absorption minima. The velocity evolution of these ions is shown in Figure 9. One can see that the velocities of hydrogen lines are higher than those of metal lines; the hydrogen lines have a lower optical depth and thus are formed at larger radii in the ejecta. The velocities seem to decline with an exponential trend.

To examine the differences of photospheric velocity between SN 2014cx and other SNe IIP, we compared the velocity as measured from the Fe II λ5169 line. As shown in Figure 10, SN 2014cx and SN 2014et have similar velocities at comparable phases, and their expansion velocities are higher than those of SN 1999em (by $\sim$1000 km s^{-1}) and SN 2005cs (by $\sim$3000 km s^{-1}).

5. PROGENITOR ESTIMATES

5.1. Radius of Progenitor

For CC SNe, following the shock breakout, the heated stellar envelope expands and then cools down. The different timescales of photospheric temperature evolution depend mainly upon the initial radius of the progenitor and the opacity. A simple analytic function has been proposed by Rabinak & Waxman (2011) to estimate the radius of the progenitor of CC SNe using the early time temperature evolution. Theoretically, the duration that the photosphere can stay at a higher temperature depends on the radius of progenitor star, with longer time for a progenitor with a larger radius (and vice versa).

We constructed the spectral energy distribution (SED) and computed the blackbody temperatures using the *Swift* UV and optical data obtained during the first week after explosion. The luminosity and temperature can then be used to constrain the

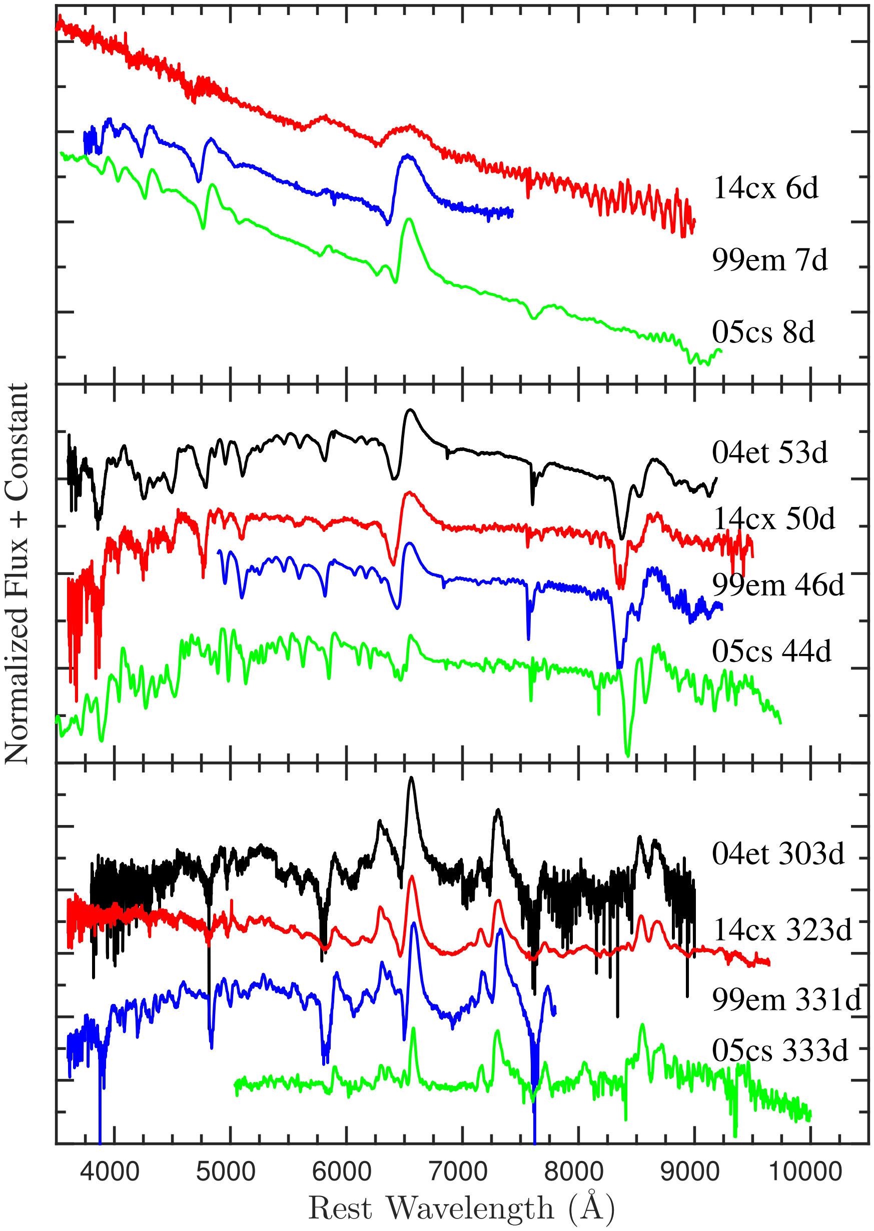

Figure 8. Comparison of the reddening- and Doppler-corrected spectra of SNe 2014cx, 2004et, 1999em, and 2005cs at similar phases. Top panel, one week after explosion; middle panel, about 50 days after explosion; bottom panel, about one year after explosion.

radius of the progenitor star by using Equation (13) of Rabinak & Waxman (2011; e.g., Valenti et al. 2014; Bose et al. 2015; Rubin et al. 2016). Note that the equation is only valid for the first week after explosion, when the light curve is dominated by shock cooling at very early phase, and the photosphere is located at the outer shell of the expanding ejecta (Rubin et al. 2016). Adopting an optical opacity of 0.34 $\mathrm{cm}^2\ \mathrm{g}^{-1}$ and a typical RSG density profile $f_\rho = 0.13$, we obtained an initial radius of $643 \pm 60\ R_\odot$ for the progenitor of SN 2014cx (see Figure 11), consistent with the typical size of an RSG.

Based on the SuperNova Explosion Code (SNEC; Morozova et al. 2015), Morozova et al. (2016) suggest that the early time evolution of the light curves of SNe IIP relies sensitively on the radius of the exploding star, as explained with an analytical correlation between the g-band rise time and the progenitor radius (i.e., $\log R\,[R_\odot] = 1.225 \log t_{\mathrm{rise}}$ [day] $+ 1.692$). Thus, we fit the early time g-band light curve of SN 2014cx and obtain the rise time as $t_{\mathrm{rise}} = 7.90 \pm 0.10$ days. Inserting this value into the rise time–radius relation, we estimate the radius of the progenitor to be $619 \pm 10\ R_\odot$.

5.2. Hydrodynamical Modeling

In this subsection, we further determine the main physical parameters of SN 2014cx and its progenitor (i.e., the explosion energy, the radius of progenitor star, and the ejected mass) using a method of hydrodynamical modeling. This method uses the SN observables (i.e., the bolometric light curve, the velocity evolution, and the temperature of the continuum obtained during the photospheric phase) as input parameters to constrain the physical properties of expanding ejecta and the evolution of SN observables (from the shock breakout up to the nebular phase) using the general-relativistic, radiation-hydrodynamics code. This technique has been successfully applied to the

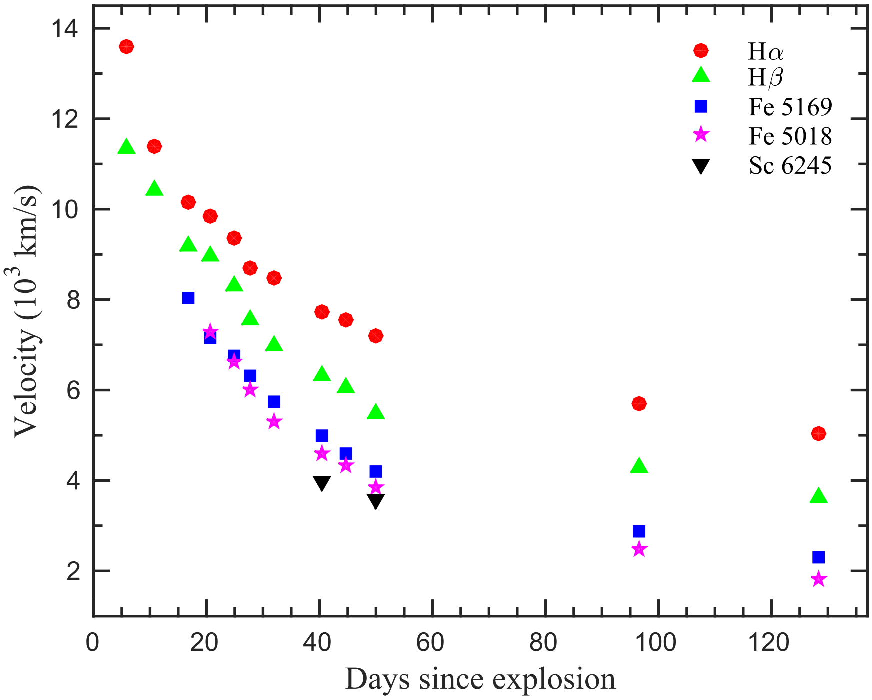

Figure 9. Velocity evolution of Hα, Hβ, and Fe II. The velocities are estimated using the Doppler shift of the absorption minima.

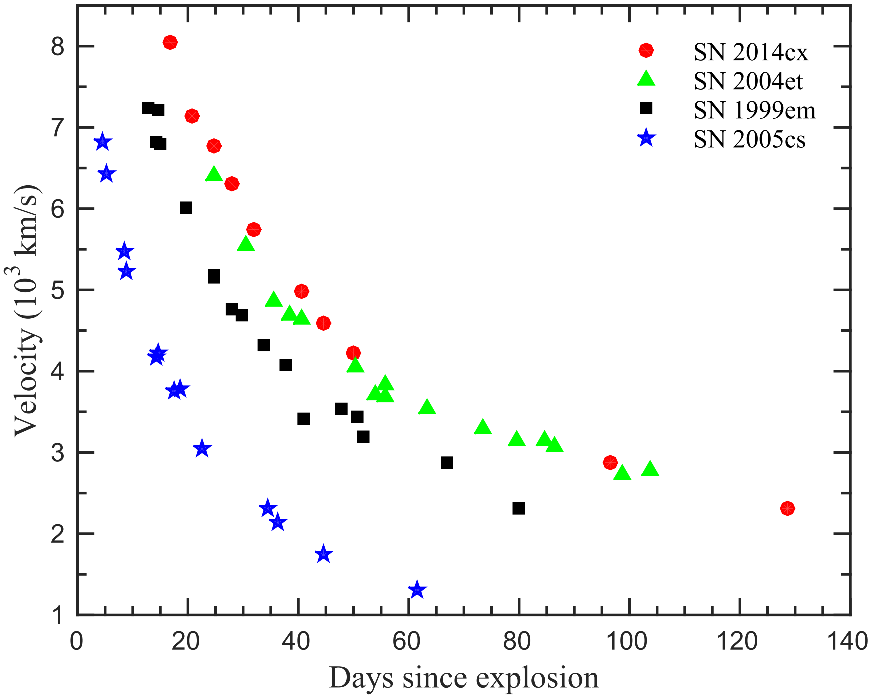

Figure 10. Comparison of the expansion velocities of SN 2014cx measured from Fe II λ5169 to those of the luminous Type IIP SN 2004et, the normal SN 1999em, and the subluminous SN 2005cs.

studies of numerous SNe IIP, including SNe 2007od, 2009bw, 2009E, 2012A, 2013ab, and 2013ej (Inserra et al. 2011, 2012; Pastorello et al. 2012; Tomasella et al. 2013; Bose et al. 2015; Huang et al. 2015). Details about this hydrodynamical model are well described in Zampieri et al. (2003), Pumo et al. (2010), and Pumo & Zampieri (2011).

Based on the estimates of the explosion epoch (MJD = 56,901.89; Section 3.1), bolometric luminosity, and nickel mass (0.056 $M_\odot$; Section 3.5), the best-fit hydrodynamic model returns a total (kinetic plus thermal) energy of 0.4×10^{51} erg, an initial radius of 4×10^{13} cm (~570 $R_\odot$), and an envelope mass of 8 $M_\odot$ (see Figure 12) for SN 2014cx. Considering a mass of ~1.5–2.0 $M_\odot$ for the compact remnant star, we estimate that SN 2014cx has an immediate progenitor mass of 9.5–10.0 $M_\odot$ when exploding. The zero-age main-sequence mass should be slightly higher given that the progenitor star suffers some mass loss during the lifetime. These values are consistent with those of a typical RSG with

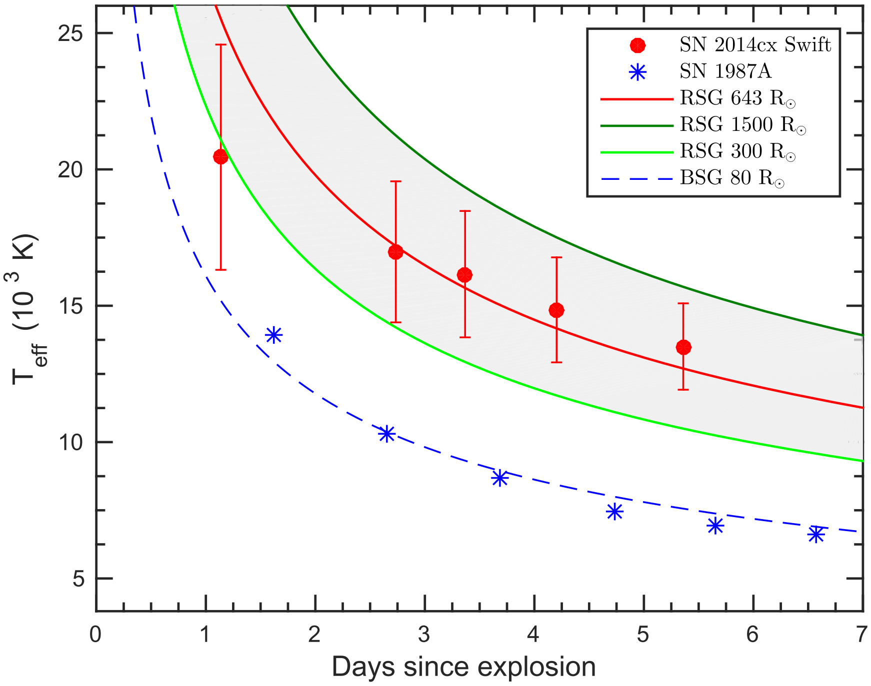

Figure 11. Constraining the progenitor radius using the Rabinak & Waxman (2011) prescription. The red solid line is the best fit for a RSG of 643 $R_\odot$, and the blue dashed line is for a BSG of 80 $R_\odot$ for SN 1987A.

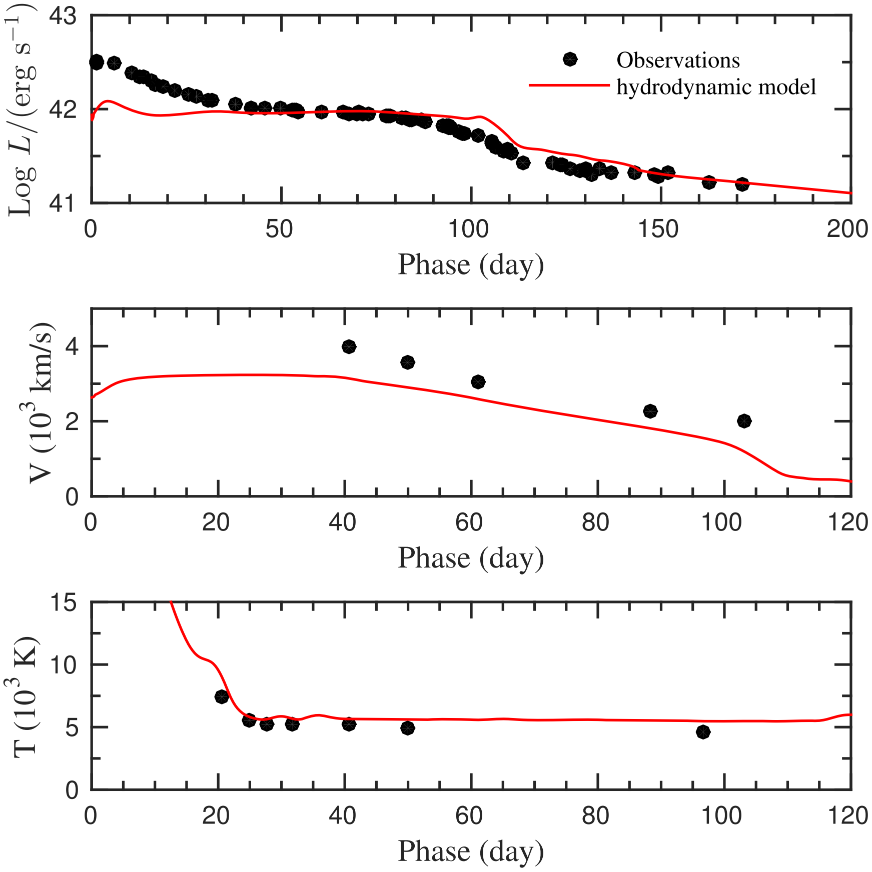

Figure 12. Comparison of the evolution of the main observables of SN 2014cx with the best-fit model computed with the general-relativistic, radiation-hydrodynamics code (total energy ~0.4 × 10^{51} erg, initial radius 4 × 10^{13} cm, envelope mass 8 $M_\odot$). Top, middle, and bottom panels show the bolometric light curve, the photospheric velocity, and the photospheric temperature as a function of time, respectively. To estimate the photospheric velocity from observations, we used the value inferred from the Fe II λ5169 line.

relatively low mass. The radius is also in agreement with that estimated from the early temperature as described in Section 5.1 within uncertainties.

We further compare our light curves and spectra with those from Kasen & Woosley (2009), and we found that our parameters generally fall into the range of their Table 2, except that we have a smaller nickel mass (0.056 $M_\odot$ versus 0.1–0.5 $M_\odot$). This difference is likely due to their numerical models using larger main-sequence masses (12–25 $M_\odot$) than our hydrodynamic modeling results (9.5–10.0 $M_\odot$).

The evolutions of three observables (luminosity, velocity, and temperature) and the modeling results are shown in Figure 12. As can be seen, the modeling reasonably matches the observed luminosity/temperature except at early phases where a larger deviation is seen in luminosity. This deviation is likely due to the density profile in the radial direction of the outermost ejecta not being well produced by our simulations (Pumo & Zampieri 2011). In the middle panel of Figure 12, we note that there is also a small ($\lesssim$10%–15%) discrepancy between our best-fit model and the observed photospheric velocity. This discrepancy may be attributed to a systematic shift between the true photospheric velocity and the values estimated from the observed P-Cygni line profiles (Dessart & Hillier 2005). This can be explained with the fact that the optical depth is higher for spectral lines relative to the continuum, which can place the line photosphere at a larger radius (see also Inserra et al. 2013). As discussed in previous work (e.g., Zampieri et al. 2003; Pumo et al. 2011; Huang et al. 2015), the early velocity evolution cannot be reproduced in our simulations and is thus excluded from the fit. The early evolution is caused by the shock-wave propagation in the outermost several percent of the pre-supernova mass. Thus, we suggest that omitting the early stages does not significantly affect our estimates of the parameters of the bulk of the ejecta. However, we are aware that our simplification requires support via detailed modeling of the full data set.

6. DISCUSSION AND SUMMARY

In this paper, we present extensive UV and optical photometry and optical spectroscopy of SN 2014cx in NGC 337, spanning the period from −30 days to +404 days from the maximum light. The explosion time is constrained to be MJD = 56,901.89 with an accuracy of ±0.5 days.

The characteristics of the light curves, such as the rise time, duration of the plateau phase, post-peak decline, and bolometric luminosity, suggest that SN 2014cx is a normal Type IIP supernova. The KAIT unfiltered and LCOGT r-band light curves seem to experience two brightening components, with the first likely related to shock breakout of the supernova. The plateau duration is ~100 days, similar to that of our comparison SNe IIP. The value of M_V at mid-plateau phase (~50 day) is -16.48 ± 0.43 mag for SN 2014cx, lying between the luminous SNe IIP (~ -17 mag, SN 2004et) and subluminous SNe IIP (~ -15 mag, SN 2005cs). The mass of ^{56}Ni, using the tail luminosity and steepness methods, is 0.056 $M_\odot$, similar to that of SN 1999em and SN 2004et.

The spectroscopic evolution of SN 2014cx shares a similarity with the typical Type IIP SNe 1999em and 2004et. The early time spectra exhibit a nearly featureless continuum with only hydrogen Balmer lines and He I visible. As the SN evolves, the continuum becomes redder and the metal lines emerge, becoming the dominant features during the photospheric phase. During the nebular phase, the spectra are dominated by strong emission lines. The continuum at 3800–5000 Å is relatively blue, which might be caused by either late time CSM interaction or a scattered-light echo. The value and evolution of the expansion velocity derived from Fe II λ5169 are similar to those of SN 2004et, but ~1000 km s^{-1} higher than the expansion velocity of SN 1999em.

By modeling the observables of SN 2014cx as derived from our observations, we estimate that this explosion produces a total energy of 0.4×10^{51} erg and an ejected mass of ~8.0 $M_\odot$. The progenitor star is calculated to have a radius of 4×10^{13} cm (~574 $R_\odot$), which agrees well with that estimated from the early photospheric temperature evolution (643 ± 60 $R_\odot$) and g-band rise time–radius relation from SNEC (619 ± 10 $R_\odot$). The values above are consistent with a core-collapse scenario from a typical RSG having an initial mass of 9.5–10 $M_\odot$.

We thank the support of the staffs at Xinglong Station (National Astronomical Observatory of China), Li-Jiang Observatory (Yunnan Astronomical Observatory of China), and Lick Observatory for assistance with the observations. We also acknowledge the use of public data from the *Swift* and Las Cumbres Observatory Global Telescope Network data archives. Some of the data presented herein were obtained at the W. M. Keck Observatory, which is operated as a scientific partnership among the California Institute of Technology, the University of California, and NASA; the observatory was made possible by the generous financial support of the W. M. Keck Foundation. KAIT and its ongoing operation were made possible by donations from Sun Microsystems, Inc., the Hewlett-Packard Company, AutoScope Corporation, Lick Observatory, the U.S. National Science Foundation (NSF), the University of California, the Sylvia & Jim Katzman Foundation, and the TABASGO Foundation. Research at Lick Observatory is partially supported by a generous gift from Google. We thank N. N. Chugai for some useful correspondence.

This work is supported by the Major State Basic Research Development Program (2013CB834903), the National Natural Science Foundation of China (NSFC grants 11178003, 11325313, and 11633002), and the Strategic Priority Research Program of Emergence of Cosmological Structures of the Chinese Academy of Sciences (grant No. XDB09000000). T.-M.Z. is supported by the NSFC (grants 11203034). J.-J.Z. is supported by the NSFC (grants 11403096), the Key Research Program of the CAS (Grant No. KJZD-EW-M06), and the CAS "Light of West China" Program. D.A.H., C.M., and G.H. are supported by NSF grant 1313484. A.V.F.'s group at UC Berkeley is grateful for financial assistance from NSF grant AST-1211916, the TABASGO Foundation, Gary and Cynthia Bengier, and the Christopher R. Redlich Fund. The work of A. V.F. was completed at the Aspen Center for Physics, which is supported by NSF grant PHY-1066293; he thanks the Center for its hospitality during the black holes workshop in 2016 June and July.

REFERENCES

Ahn, C. P., Alexandroff, R., Allende Prieto, C., et al. 2012, ApJS, 203, 21
Anderson, J. P., González-Gaitán, S., Hamuy, M., et al. 2014, ApJ, 786, 67
Andrews, J., Smith, N., Fong, W.-f., & Milne, P. 2015, ATel, 7084, 1

Andrews, J. E., Krafton, K. M., Clayton, G. C., et al. 2016, MNRAS, 457, 3241
Arcavi, I., Gal-Yam, A., Cenko, S. B., et al. 2012, ApJL, 756, L30
Arnett, D. 1996, Supernovae and Nucleosynthesis: An Investigation of the History of Matter, from the Big Bang to the Present, ed. D. Arnett, (Princeton: Princeton Univ. Press)
Barbon, R., Ciatti, F., & Rosino, L. 1979, A&A, 72, 287
Bose, S., Valenti, S., Misra, K., et al. 2015, MNRAS, 450, 2373
Breeveld, A. A., Landsman, W., Holland, S. T., et al. 2011, in AIP Conf. Ser. 1358, An Updated Ultraviolet Calibration for the Swift/UVOT, ed. J. E. McEnery, J. L. Racusin, & N. Gehrels (Melville, NY: AIP), 373
Brown, P. J., Breeveld, A. A., Holland, S., Kuin, P., & Pritchard, T. 2014, Ap&SS, 354, 89
Brown, P. J., Holland, S. T., Immler, S., et al. 2009, AJ, 137, 4517
Brown, T. M., Baliber, N., Bianco, F. B., et al. 2013, PASP, 125, 1031
Cardelli, J. A., Clayton, G. C., & Mathis, J. S. 1989, ApJ, 345, 245
Dall'Ora, M., Botticella, M. T., Pumo, M. L., et al. 2014, ApJ, 787, 139
Dessart, L., & Hillier, D. J. 2005, A&A, 439, 671
Dessart, L., Livne, E., & Waldman, R. 2010, MNRAS, 408, 827
Dhungana, G., Kehoe, R., Vinko, J., et al. 2016, ApJ, 822, 6
Elias-Rosa, N., Tartaglia, L., Cappellaro, E., et al. 2014, ATel, 6440, 1
Elmhamdi, A., Danziger, I. J., Chugai, N., et al. 2003, MNRAS, 338, 939
Falk, S. W., & Arnett, W. D. 1977, ApJS, 33, 515
Faran, T., Poznanski, D., Filippenko, A. V., et al. 2014a, MNRAS, 442, 844
Faran, T., Poznanski, D., Filippenko, A. V., et al. 2014b, MNRAS, 445, 554
Filippenko, A. V. 1997, ARA&A, 35, 309
Filippenko, A. V., Li, W. D., Treffers, R. R., & Modjaz, M. 2001, in IAU Coll. 183, Small Telescope Astronomy on Global Scales, Vol. 246, ed. B. Paczynski, W.-P. Chen, & C. Lemme (San Francisco, CA: ASP), 121
Ganeshalingam, M., Li, W., Filippenko, A. V., et al. 2010, ApJS, 190, 418
Garnavich, P. M., Tucker, B. E., Rest, A., et al. 2016, ApJ, 820, 23
Gezari, S., Jones, D. O., Sanders, N. E., et al. 2015, ApJ, 804, 28
González-Gaitán, S., Tominaga, N., Molina, J., et al. 2015, MNRAS, 451, 2212
Hamuy, M. 2003, ApJ, 582, 905
Heger, A., Fryer, C. L., Woosley, S. E., Langer, N., & Hartmann, D. H. 2003, ApJ, 591, 288
Holoien, T. W.-S., Prieto, J. L., Kochanek, C. S., et al. 2014, ATel, 6436, 1
Horne, K. 1986, PASP, 98, 609
Huang, F., Li, J.-Z., Wang, X.-F., et al. 2012, RAA, 12, 1585
Huang, F., Wang, X., Zhang, J., et al. 2015, ApJ, 807, 59
Inserra, C., Pastorello, A., Turatto, M., et al. 2013, A&A, 555, A142
Inserra, C., Turatto, M., Pastorello, A., et al. 2011, MNRAS, 417, 261
Inserra, C., Turatto, M., Pastorello, A., et al. 2012, MNRAS, 422, 1122
Kasen, D., & Woosley, S. E. 2009, ApJ, 703, 2205
Klein, R. I., & Chevalier, R. A. 1978, ApJL, 223, L109
Leonard, D. C., Filippenko, A. V., Gates, E. L., et al. 2002, PASP, 114, 35
Li, W., Leaman, J., Chornock, R., et al. 2011, MNRAS, 412, 1441
Li, W., Wang, X., Van Dyk, S. D., et al. 2007, ApJ, 661, 1013
Maguire, K., Di Carlo, E., Smartt, S. J., et al. 2010, MNRAS, 404, 981
Monet, D. 1998, USNO-A2.0 (Washington, DC: USNO)
Morozova, V., Piro, A. L., Renzo, M., et al. 2015, ApJ, 814, 63
Morozova, V., Piro, A. L., Renzo, M., & Ott, C. D. 2016, ApJ, 829, 109
Morrell, N., Marion, G. H., Kirshner, R. P., Hsiao, E. Y., & Stritzinger, M. 2014, ATel, 6442, 1
Nadyozhin, D. K. 2003, MNRAS, 346, 97
Nakano, S., Itagaki, K., Yusa, T., et al. 2014, CBET, 3963, 1
Olivares, E. F., Hamuy, M., Pignata, G., et al. 2010, ApJ, 715, 833
Pastorello, A., Pumo, M. L., Navasardyan, H., et al. 2012, A&A, 537, A141
Pastorello, A., Valenti, S., Zampieri, L., et al. 2009, MNRAS, 394, 2266
Patat, F., Barbon, R., Cappellaro, E., & Turatto, M. 1994, A&A, 282, 731
Pumo, M. L., & Zampieri, L. 2011, ApJ, 741, 41
Pumo, M. L., & Zampieri, L. 2013, MNRAS, 434, 3445
Pumo, M. L., Zampieri, L., & Turatto, M. 2010, MSAIS, 14, 123
Quimby, R. M., Wheeler, J. C., Höflich, P., et al. 2007, ApJ, 666, 1093
Rabinak, I., & Waxman, E. 2011, ApJ, 728, 63
Roming, P. W. A., Kennedy, T. E., Mason, K. O., et al. 2005, SSRv, 120, 95
Rubin, A., Gal-Yam, A., De Cia, A., et al. 2016, ApJ, 820, 33
Sahu, D. K., Anupama, G. C., Srividya, S., & Muneer, S. 2006, MNRAS, 372, 1315
Sanders, N. E., Soderberg, A. M., Gezari, S., et al. 2015, ApJ, 799, 208
Schawinski, K., Justham, S., Wolf, C., et al. 2008, Sci, 321, 223
Schlafly, E. F., & Finkbeiner, D. P. 2011, ApJ, 737, 103
Smartt, S. J. 2009, ARA&A, 47, 63
Smartt, S. J., Eldridge, J. J., Crockett, R. M., & Maund, J. R. 2009, MNRAS, 395, 1409
Sorce, J. G., Tully, R. B., Courtois, H. M., et al. 2014, MNRAS, 444, 527
Tomasella, L., Cappellaro, E., Fraser, M., et al. 2013, MNRAS, 434, 1636
Tominaga, N., Blinnikov, S., Baklanov, P., et al. 2009, ApJL, 705, L10
Valenti, S., Howell, D. A., Stritzinger, M. D., et al. 2016, MNRAS, 459, 3939
Valenti, S., Sand, D., Pastorello, A., et al. 2014, MNRAS, 438, L101
Wang, X., Li, W., Filippenko, A. V., et al. 2008, ApJ, 675, 626
Zampieri, L., Pastorello, A., Turatto, M., et al. 2003, MNRAS, 338, 711